Automatic prostate cancer detection through DCE-MRI images: all you need is a good normalization

Guillaume Lemaître, Robert Martí, and Fabrice Meriaudeau

***Abstract*—Multiparametric Magnetic Resonance Imaging (MRI) (mp-MRI) plays a major role in the detection of Prostate Cancer (PCa) and is commonly used in the design of new Computer-Aided Detection and Diagnosis (CAD) systems. Dynamic Contrast-Enhanced (DCE)-MRI is one of the modalities regularly used in mp-MRI CAD systems. Pharmocokinetic parameters are extracted from the DCE-MRI sequences and are later used to discriminate cancerous tissue from healthy tissue. However, some inter-patients variations occur during the data acquisition leading to estimation errors of the pharmacokinetic parameters. Therefore, we propose a fully automatic normalization method for DCE-MRI that reduces the inter-patients variability of the data. The benefit and simplicity of our approach is shown by detecting cancerous voxels from healthy voxels using a normalized enhanced DCE-MRI signal and comparing it with state-of-the-art quantitative and semi-quantitative methods. Additionally, we show that using this normalization approach in conjunction with the quantitative methods improves the classification performance of most of the models. The best classification performance for detecting PCa is obtained using the whole DCE-MRI normalized signal, reaching an Area Under the Curve (AUC) of 0.666 (± 0.154) and outperforming the quantitative approaches.**

***Index Terms*—DCE-MRI, prostate cancer, normalization, classification.**

I. Introduction

Prostate Cancer (PCa) is the second most frequently diagnosed cancer in men, accounting for 899,000 cases and leading to 258,100 deaths per year [1]. As highlighted by the PI-RADS Steering Committee, the two main challenges to be addressed are [2]: (i) improving the detection of clinically significant PCa and (ii) increasing confidence in benign or dormant cases and therefore avoiding unnecessary invasive medical exams. In this regard, multiparametric Magnetic Resonance Imaging (MRI) (mp-MRI) is frequently used to build robust Computer-Aided Detection and Diagnosis (CAD) systems to detect, localize, and grade PCa. In general, CAD systems are based on mp-MRI which potentially combines several of the following modalities [3]: T_2 Weighted (T_2-W)-MRI, Dynamic Contrast-Enhanced (DCE)-MRI, Apparent Diffusion Coefficient (ADC) maps, and Magnetic Resonance Spectroscopy Imaging (MRSI).

In DCE-MRI, a contrast media is injected intravenously and a set of images is acquired over time. Consequently, each voxel in an image corresponds to a dynamic signal that is related to both contrast agent concentration and the vascular properties of the tissue. Therefore, changes in the enhanced signal allows for the discrimination of healthy tissues from PCa tissues. In fact, these properties are automatically extracted using quantitative or semi-quantitative approaches [3].

Quantitative approaches uses pharmacokinetic modelling based on a bicompartment model, namely Brix [4] and Tofts [5] models. The parameters of the Brix model are inferred by assuming a linear relationship between the media concentration and the MRI signal intensity. However, this assumption has been shown to lead to inaccurate estimations of the pharmacokinetic parameters [6]. In contrast, the Tofts model requires the conversion of MRI signal intensity to concentration, which becomes a non-linear relationship using a specific equation of MRI sequences (e.g., FLASH sequence). Tofts modeling, however, is highly complex [7]. Achieving the conversion using the non-linear approach requires the acquisition of a T_1 map which is not always possible during clinical examination. Additionally, the parameter calculation requires the Arterial Input Function (AIF) which is challenging to measure and can also lead to an inaccurate estimation.

Semi-quantitative approaches are mathematical rather than pharmacokinetic because no pharmacokinetic assumptions regarding the relationship between the MRI signal and the contrast agent are made [7, 8]. These methods are advantageous because they do not require any knowledge of the MRI sequence or any conversion from signal intensity to concentration. However, they present some limitations: the heuristic approach proposed by Huisman et al. requires an initial estimate of the standard deviation of the signal noise and some manual tuning [8].

Nevertheless, all of the presented methods suffer from the following two major drawbacks: (i) inter-patient variability and (ii) loss of information. The inter-patient variability is mainly due to the acquisition process and consequently leads to generalization issues in applying a machine learning algorithm. All previous methods extract few discriminative parameters to describe the DCE-MRI signal which might lead to a loss of information.

In this work, we propose a fully automatic normalization method for DCE-MRI that reduces the inter-patient variability

G. Lemaître is with CDS Paris-Saclay, Parietal team, Inria, CEA, Université Paris-Saclay, 1 Rue Honoré d'Estienne d'Orves, 91120 Palaiseau, France e-mail: guillaume.lemaitre@inria.fr

R. Martí is with ViCOROB, Universitat de Girona, Campus Montilivi, Edifici P4, 17071 Girona, Spain.

F. Mériaudeau is with CISIR, Electrical & Electronic Engineering Department, Universiti Teknologi Petronas, 32610 Seri Iskandar, Perak, Malaysia.

Manuscript received April 29, 2017

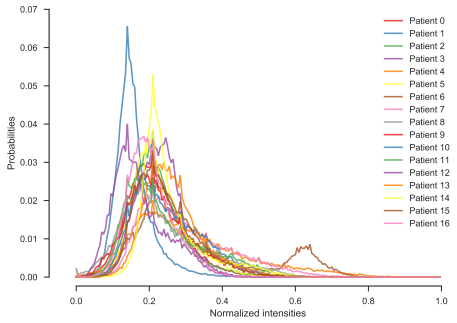

Fig. 1. Illustration of the inter-patient variations in 17 different patients in T_2-W-MRI, using the PDF representation.

of the data. The benefit and simplicity of our approach will be demonstrated by classifying the whole normalized DCE-MRI signal and comparing it with state-of-the-art quantitative and semi-quantitative methods. Additionally, we will show that using this normalization approach in conjunction with the quantitative methods improves the classification performance of most of the models. We also propose a new clustering-based method to discern enhanced signals from the arteries that can, later be used to estimate an AIF and provide an alternative approach to estimate the parameters of the semi-quantitative model proposed by [8].

The paper is organized as follows: Section II-A details our normalization strategy for the DCE-MRI data. Quantitative and semi-quantitative methods are summarized in Sect. II-B with insights about their implementations. Section III provides information about the dataset used and the provided source code. Experiments and results that address the previously stated challenges are reported in Sect. IV and discussed in Sect. V, followed by a concluding section.

II. Methods

A. Normalization of DCE-MRI images

In this work, we propose a method to normalize DCE-MRI prostate data to reduce inter-patient variations, although this method can be applied to any DCE-MRI sequences. In T_2-W-MRI, these variations are characterized by a shift and a scaling of the intensities as illustrated by the intensity Probability Density Function (PDF) in Fig. 1. Therefore, these variations can be corrected using a z-score approach,— i.e., normalizing the data by subtracting the mean and dividing by the standard deviation —assuming that the data follow a specific distribution [9].

In DCE-MRI, the intensity PDF of the prostate gland does not follow a unique type of distribution such as Rician or Gaussian distribution, as shown in Fig. 2a. Indeed, the inter-patient variations are more complex due to the temporal acquisition. A better means of observing these variations is to represent the intensity PDF of the prostate gland over time—, requiring segmentation of the prostate —using a heatmap representation as shown in Fig. 2a. By analyzing this heatmap representation across patients (see Fig. 2c), the following variations are highlighted: (i) intensity offsets (Δ_i) of the PDF peak, (ii) a time offset (Δ_t) depending on the contrast agent arrival, and (iii) a change of scale (α_i) related to the signal enhancement. Therefore, our normalization method should attenuate all of these variations and be performed globally across the different time sequences rather than for each independent sequence.

1) Graph-based intensity offsets correction: Before standardizing each sequence, the first step of the normalization process is to cancel the intensity specific at each patient, which occurs due to the media injection. As previously mentioned, the intensity PDF does not always follow a Rician or a Gaussian distribution over time, in DCE-MRI. Therefore, the mean of these distributions cannot be used as a potential estimate for these offsets. Additionally, these offsets should be characterized by a smooth transition between series over time. Thus, this problem is solved using the graph-theory: considering the intensity PDF over time as shown in Fig. 2a, the offsets correspond to the boundary splitting, the heatmap into two partitions such that they are as close as possible to the peak of the intensity PDF (see Fig. 3 for an illustration). Given the heatmap, a directed weighted graph $\mathcal{G} = (\mathcal{V}, \mathcal{E})$ is built by taking each bar—, i.e., the probability for a given time and pixel intensity—, of the heatmap as a node and connecting each pair of bars by an edge. The edge weight w_{ij} between two nodes i and j corresponds to two pixels at positions (x_i, y_i) and (x_j, y_j), respectively, is defined as in Eq. (1), as follows:

$$w_{ij} = \begin{cases} \alpha \exp(1 - \frac{H(i)}{\max(H)}) & \text{if } x_j = x_i + 1 \text{ and } y_j = y_i, \\ (1-\alpha) \exp(1 - \frac{H(i)}{\max(H)}) & \text{if } x_j = x_i \text{ and } y_j = y_i + 1, \\ 0 & \text{otherwise,} \end{cases} \tag{1}$$

where H is the heatmap, and α is a smoothing parameter controlling for the partitioning.

Therefore, these offsets related to Δ_i are estimated by finding the shortest-path to cross the graph using Dijkstra's algorithm. The entry and exiting nodes are set to be the bin with the maximum probability for the first value in the DCE-MRI series and the bin corresponding to the median value for the last value of the DCE-MRI series, respectively. To ensure a robust estimation of these offsets, the process of finding the shortest-path is repeated by shifting the data and updating the heatmap as well as the graph $\mathcal{G}$. The procedure is stopped once the offset found does not change. In general, this process is not repeated more than 3 times. The parameter α is set to 0.9, empirically. Figure 3 illustrates the final estimation of the offsets, Δ_i (i.e., red landmark), found for each value of the DCE-MRI series. Therefore, each intensity offset is subtracted for each DCE-MRI.

2) Time offset and data dispersion correction: The next variations to correct are the time offset, Δ_t, and the data dispersion, σ_i. By computing the Root-Mean-Square Deviation (RMSD) of the intensities for each value of the DCE-MRI series, one can observe these two variations as shown in Fig. 4a. Therefore, to correct these variations, we propose the registration of each patient RMSD to a mean model that corresponds to the mean of all patients' RMSD values. The parametric model required to perform the registration is formulated in Eq. (2), as follows:

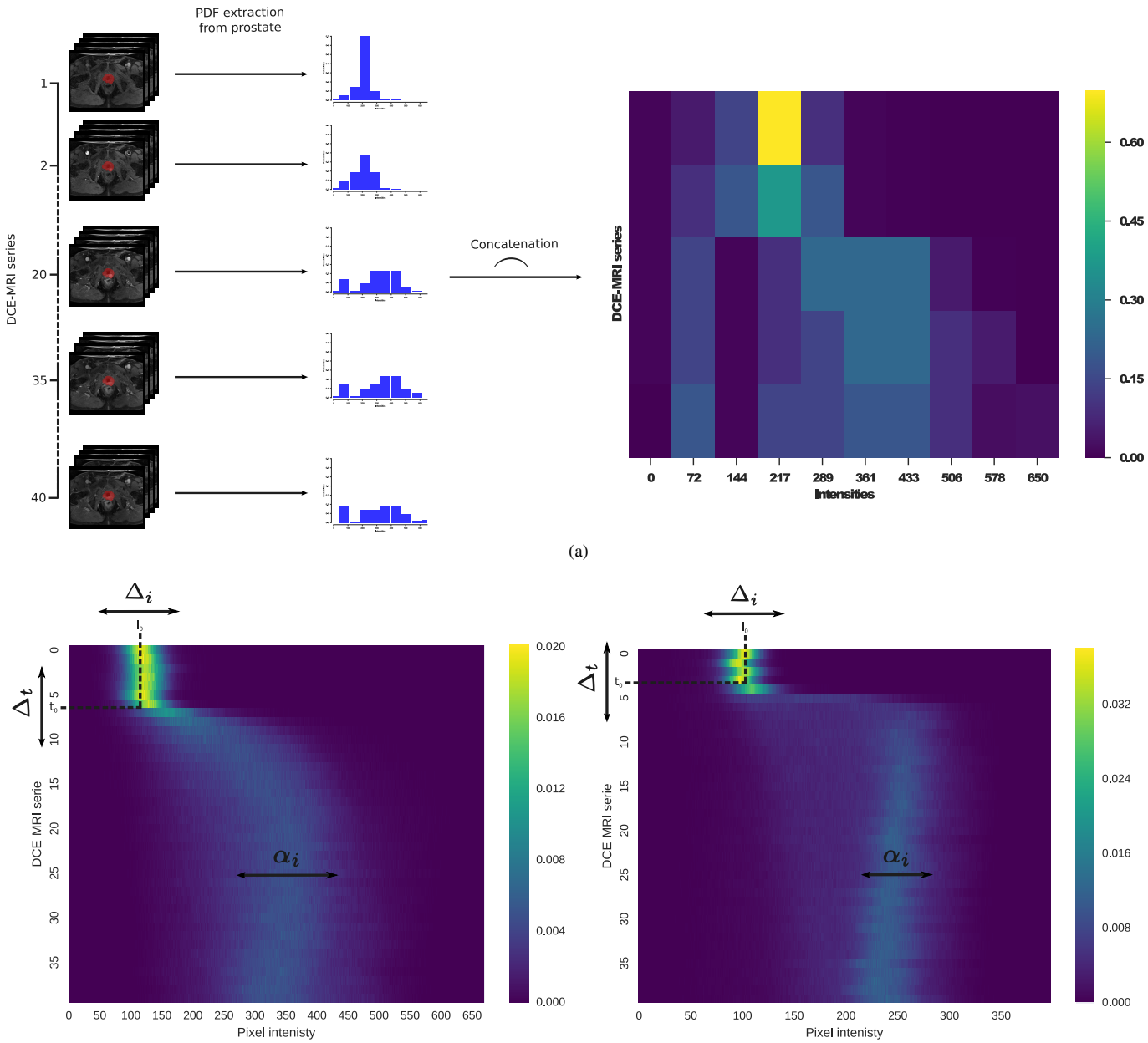

(a)

(b) I_0: 117; t_0: 6$^{\text{th}}$ serie; wider st. dev.

(c) I_0: 103; t_0: 4$^{\text{th}}$ serie; narrower std. dev.

Fig. 2. (a) Illustration of the heatmap representation: all PDFs of the prostate gland are concatenated together to build an heatmap; (b)-(c) Heatmap of 2 patients revealing the three types of inter-patient variations: intensity shift (Δ_i), time shift (Δ_t), and intensity scale (α_i).

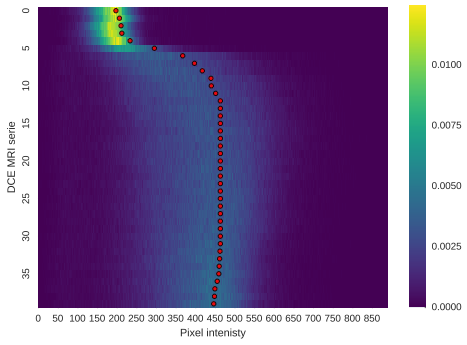

Fig. 3. Illustration of the estimator found using the shortest-path through the graph.

$$T(\alpha, \tau, f(t)) = \alpha f(t - \tau), \tag{2}$$

where α and τ are the two parameters handling the time offset Δ_i and the global scale σ_i, respectively, $f(\cdot)$ is the RMSD function defined as follows:

$$f(t) = \sqrt{\left(\frac{\sum_{n=1}^{N} x(t)_n^2}{N}\right)}, \tag{3}$$

where $x(t)_n$ is the shifted intensity of a sample from a specific DCE-MRI series value at time t from a total number of N samples.

Therefore, the registration problem is equivalent to:

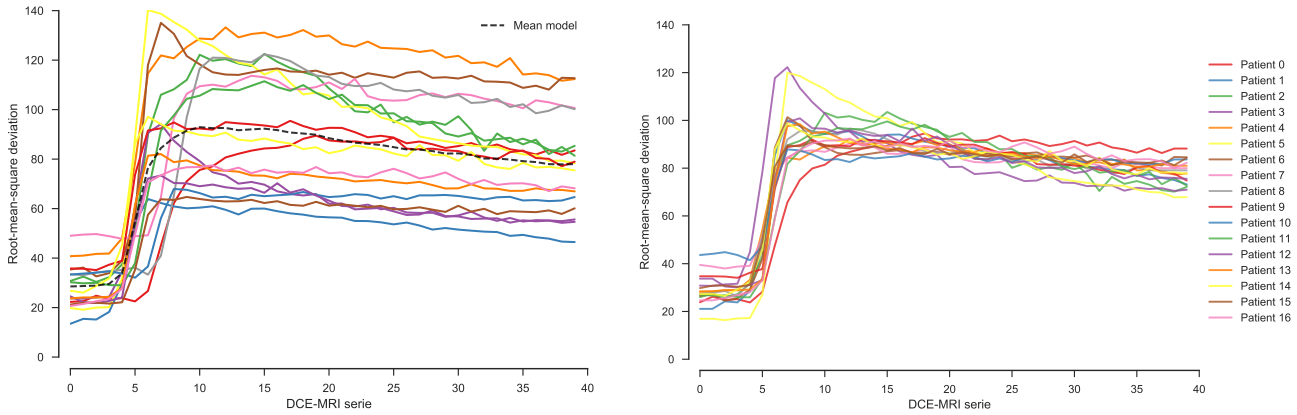

(a) RMSD computed for each patient of our dataset.

(b) RMSD after alignment using the curve parametric model.

Fig. 4. Illustration of the correction of the time offset and the data dispersion.

$$\arg\min_{\alpha,\tau} = \sum_{t=1}^{N} \left[T\left(\alpha, \tau, f(t)\right) - \mu(t)\right]^2, \tag{4}$$

where $\mu(\cdot)$ is the mean model and, N is the number of values in the DCE-MRI series.

An illustration of the correction applied to each RMSD of the patients is shown in Fig. 4b. Once all of these parameters have been determined, the data are shifted and scaled.

The resulting normalized data can be used into two ways: (i) each normalized signal can be used as a whole to determine if the corresponding voxel is healthy or cancerous or (ii) the normalized data can be fitted using a quantitative method, as presented in the next section.

B. Quantification of DCE-MRI

In this section, we summarize the different methods that have been used for the quantification of DCE-MRI for PCa detection [3] and will be used for comparison in this work. Furthermore, we would like to emphasize the following additional contributions for this section: (i) a novel automatic AIF estimation algorithm based on clustering and (ii) a simplified semi-quantitative method using constrained optimization.

1) Brix and Hoffmann models: In the Brix model [4], the MRI signal intensity is assumed to be proportional to the media concentration. Therefore, the model is expressed as shown in Eq. (5), as follows:

$$s_n(t) = 1 + A\left[\frac{\exp(k_{el}t') - 1}{k_{ep}(k_{ep} - k_{el})}\exp(-k_{el}t) - \frac{\exp(k_{ep}t') - 1}{k_{el}(k_{ep} - k_{el})}\exp(-k_{ep}t)\right], \tag{5}$$

with

$$s_n(t) = \frac{s(t)}{S_0}, \tag{6}$$

where $s(t)$ and S_0 are the MRI signal intensity at time t and the average pre-contrast MRI signal intensity, respectively; A, k_{el}, and k_{ep} are the constant proportional to the transfer constant, the diffusion rate constant, and the rate constant, respectively. Additionally, t' is set such that $0 \leq t \leq \tau$, $t' = t$ and so forth while $t > \tau$, $t' = \tau$.

Hoffmann et al. proposed a similar model, expressed in Eq. (7), which is derived from the Brix model:

$$s_n(t) = 1 + \frac{A}{\tau}\left[\frac{k_{ep}\left(\exp(k_{el}t') - 1\right)}{k_{el}(k_{ep} - k_{el})}\exp(-k_{el}t) - \frac{\exp(k_{ep}t') - 1}{(k_{ep} - k_{el})}\exp(-k_{ep}t)\right], \tag{7}$$

where the constant A is redefined by isolating the parameter τ.

The parameters A, k_{el}, and k_{ep} are estimated by fitting the model using non-linear least-squares optimization solved with Levenberg-Marquardt algorithm.

2) Tofts model: The extended Tofts model is formulated as shown in Eq. (8), as follows:

$$C_t(t) = K_{trans}C_p(t) * \exp(-k_{ep}t) + v_pC_p(t), \tag{8}$$

where $*$ is the convolution operator; $C_t(t)$ and $C_p(t)$ are the concentrations of contrast agent in the tissue and in the plasma, respectively; K_{trans}, k_{ep}, and v_p are the volume transfer constant, the diffusion rate constant, and the plasma volume fraction, respectively.

Therefore, the Tofts model requires: (i) detection of the candidate voxels from the femoral or iliac arteries and an estimation of a patient-based AIF signal, (ii) conversion of the MRI signal intensity (i.e., AIF and dynamic signal) to a concentration, and (iii) in the case of a population-based AIF, an estimation of an AIF signal.

Segmentation of artery voxels and AIF estimation The AIF signal from DCE-MRI can be manually estimated by selecting the most-enhanced voxels from the femoral or iliac arteries [11]. Few methods have been proposed to address the automated extraction of the AIF signal. Chen et al. successively filtered the possible candidates to be considered as the AIF such that [12]: (i) dynamic signals with a small peak and voxels with a small wash-in are

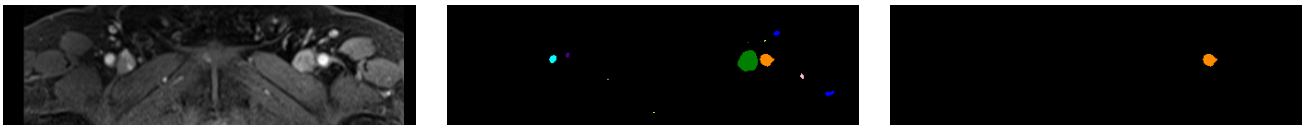

(a) Original image. (b) Candidates region after clustering. (c) Regions selected after applying the different criteria.

Fig. 5. Illustration of the segmentation of the area used to determine the AIF.

rejected by thresholding, (ii) a blob detector is used and large enough regions are maintained, and (iii) circular and cylindricality criteria are used to reject the false positives. Zhu et al. proposed an iterative method that involves the selection of voxels that best fit a gamma variate function [13]. However, this method requires the computation of the first and second derivatives as well as the maximum curvature points. Shanbhag et al. proposed the following 4-step algorithm [14, 15]: (i) remove the slices with artifacts and find the best slices based on intrinsic anatomic landmarks and enhancement characteristics, (ii) find the voxel candidates using the maximum enhanced voxels and a multi-label maximum entropy based thresholding algorithm, (iii) exclude the region next to the endorectal coil, and (iv) select the best 5 candidates that meet the enhancement characteristics and are correlated.

All the above methods are rather complex, therefore, we propose a simpler method that is based on the following reasonable assumptions: (i) all possible AIF signal candidates should have a similar shape, (ii) they should all have high enhancement, and (iii) the arteries should be almost round and within a size range. Therefore, each slice is clustered into regions using K-means clustering with $k = 6$. The cluster made of the most enhanced signals is selected since it contains the artery signals. In this regards, the selection criteria corresponds to the 90$^{\text{th}}$ percentile of the maximum DCE-MRI signal. Finally, regions with an eccentricity smaller than 0.5 and an area in the range of $[100, 400]$ voxels are kept. Additionally, to remove voxels contaminated by the partial volume effect, only the 10% most enhanced voxels of the possible candidates are kept as proposed by [16] and the average signal is computed. A summary of the different segmentation steps is presented in Fig. 5.

Conversion of MRI signal intensity to concentration

To estimate the free parameters of the Tofts model (see Eq. (8)), the concentrations $C_t(t)$ and $C_p(t)$ need to be computed from the MRI signal intensity and the AIF signal, respectively. This conversion is based on the equation of the FLASH sequence—see A for details—and is formulated as in Eq. (9):

$$c(t) = \frac{1}{TR \cdot r_1} \ln\left(\frac{1 - \cos\alpha \cdot S^* \frac{s(t)}{S_0}}{1 - S^* \frac{s(t)}{S_0}}\right) - \frac{R_{10}}{r_1}, \quad (9)$$

with,

$$S^* = \frac{1 - \exp(-TR \cdot R_{10})}{1 - \cos\alpha \cdot \exp(-TR \cdot R_{10})}, \quad (10)$$

where $s(t)$ is the MRI signal, S_0 is the MRI signal prior to the injection of the contrast media, α is the flip angle, TR is the Repetition Time (TR), R_{10} is the pre-contrast tissue relaxation time also equal to $\frac{1}{T_{10}}$, and r_1 is the relaxivity coefficient of the contrast agent.

T_{10} can be estimated from the acquisition of a T_1 map. However, this modality is not part of the clinical trial in this research and the value of T_{10} is fixed to $1600\,\mathrm{ms}$ for both blood and prostate, in accordance with the values found in the literature [15, 17, 18].

Estimation of population-based AIF While estimating the pharmacokinetic parameters using the Tofts model, the AIF concentration $C_p(t)$ can be computed either from the patient or a population. In the two previous sections, we presented the algorithms that allow for the estimation of the patient-based AIF concentration. For a comparison with the previous approach, we also computed a population-based AIF that will be used later to compare the performance of both approaches. In this regard, the population-based AIF was estimated in accordance with the method of [11] by fitting the average patient-based AIFs to the model of [19] which is formulated as shown in Eq. (11), as follows:

$$C_p(t) = \sum_{n=1}^{2} \frac{A_n}{\sigma_n\sqrt{2\pi}} \exp\left(\frac{-(t - T_n)^2}{2\sigma_n^2}\right) + \frac{\alpha \exp(-\beta t)}{1 + \exp - s(t - \tau)}, \quad (11)$$

where A_n, T_n, and σ_n are the scaling constants, centers, and widths of the n$^{\text{th}}$ Gaussian, respectively; α and β are the amplitude and decay constant of the exponential, respectively; and s and τ are the width and center of the sigmoid function, respectively.

The parameters are estimated by fitting the model using constrained non-linear least-squares optimization, solved with the Trust Region Reflective algorithm [20] and bounding the parameters to be positive.

3) PUN model: Gliozzi et al. showed that the Phenomenological Universalities (PUN) approach can be used for DCE-MRI analysis [7]. The model has been successfully used in a CAD system proposed by [21]. This model can be expressed as in Eq. (12):

$$s_n(t) = \exp\left[rt + \frac{1}{\beta}(a_0 - r)(\exp(\beta t) - 1)\right], \quad (12)$$

with

$$s_n(t) = \frac{s(t) - S_0}{S_0}, \quad (13)$$

where $s(t)$ and S_0 are the MRI signal intensity at time t and the average pre-contrast MRI signal intensity, respectively; and r, a_0, and β are the free parameters of the model.

The parameters are estimated by fitting the model using non-linear least-squares optimization solved with Levenberg-Marquardt algorithm.

4) Semi-quantitative analysis: The semi-quantitative analysis of the DCE-MRI is equivalent to extracting curve characteristics directly from the signal without a strict theoretical pharmacokinetic meaning. In this work, we use the model presented by [8], which formulates the MRI signal as in Eq. (14):

$$s(t) = \begin{cases} S_0 & 0 \leq t \leq t_0 \\ S_M - (S_M - S_0)\exp\left(\frac{-(t-t_0)}{\tau}\right) & t_0 < t \leq t_0 + 2\tau \\ S_M - (S_M - S_0)\exp\left(\frac{-(t-t_0)}{\tau}\right) + w(t - t_0 + 2\tau) & t > t_0 + 2\tau \end{cases} \tag{14}$$

where $s(t)$ is the MRI signal intensity, S_0 is the pre-contrast signal intensity, t_0 is the time corresponding to the start of enhancement, S_M and τ are the maximum of the signal and the exponential time constant, respectively, and w is the slope of the linear part.

Huisman et al. argue that curve fitting via least-squares minimization using the Nelder-Mead algorithm leads to inaccurate estimations of the parameters free parameters. Mainly the issue comes from an incorrect estimation of the start of enhancement t_0, leading to an incorrect estimation of the other parameters. Therefore, Huisman et al. to (i) robustly estimate t_0, (ii) estimate S_0 by averaging the samples between 0 and t_0, (ii) estimate w depending on whether the slope is significant or not, and (iii) estimate S_M, which should be the point of intersection of the most probable slope line and the plateau.

Instead of these successive estimations, we propose a unified optimization in which t_0 is fixed since it is a key parameter. Therefore, t_0 is robustly estimated from the AIF signal since this is the most enhanced signal in which the start of enhancement is easily identifiable. The AIF signal is computed as discussed in Section II-B2. t_0 is estimated by finding the maximum of the first derivative of the AIF signal, always occurring at the beginning of the signal. Then, the function in Eq. (14) is fitted using non-linear least squares with the Trust Region Reflective algorithm [20]. Furthermore, the parameters τ and S_M are bounded during the optimization to ensure robust estimations. τ is bounded between t_0 and t_f, which is the time of the last sample, and S_M is bounded between S_0 and $\max(s(t))$.

From Eq. (14), the following features can be extracted: (i) the wash-in corresponding to the slope between t_0 and $t_0+2\tau$, (ii) the wash-out corresponding to the parameter w, (iii) the area under the curve between t_0 and the end of the signal, (iv) the exponential time constant τ, and (v) the relative enhancement of $S_M - S_0$.

III. Materials

A. Data

The multi-parametric MRI data are acquired from a cohort of patients with higher-than-normal levels of Prostate-Specific Antigen (PSA). Acquisition is achieved with a 3T whole body MRI scanner (Siemens Magnetom Trio TIM, Erlangen, Germany) using sequences to obtain T_2-W-MRI, DCE-MRI and Diffusion Weighted (DW)-MRI. In addition to the MRI examination, these patients also have undergone a Transrectal UltraSound (TRUS) guided-biopsy. The dataset is composed of a total of 20 patients, 18 of which have biopsies that were positive for PCa and 2 patients are considered "healthy" because they have negative biopsies. Therefore, 13 patients have PCa in the Peripheral Zone (PZ), 3 patients have PCa in the Central Gland (CG), 2 patients have invasive PCa in both the PZ and the CG, and finally 2 patients are considered "healthy". An experienced radiologist segmented the prostate organ—on T_2-W-MRI and DCE-MRI—as well as the prostate zones (i.e., PZ and CG) and the PCa on the T_2-W-MRI.

A $3\,\mathrm{mm}$ slice of fat-suppressed T_2-W fast spin-echo sequence (TR/Echo Time (TE)/Echo Train Length (ETL): $3400\,\mathrm{ms}/85\,\mathrm{ms}/13$) is used to acquire images in the sagittal and oblique coronal planes, with the latter planes orientated perpendicular or parallel to the prostate PZ rectal wall axis. Three-dimensional T_2-W fast spin-echo (TR/TE/ETL: $3600\,\mathrm{ms}/143\,\mathrm{ms}/109$, slice thickness: $1.25\,\mathrm{mm}$) images are then acquired in an oblique axial plane. The nominal matrix and the Field Of View (FOV) of the 3D T_2-W fast spin-echo images are 320×256 and 280×240 mm^2, respectively, thereby affording sub-millimetric pixel resolution within the imaging plane.

DCE-MRI is performed using a fat-suppressed 3D T_1 VIBE sequence (TR/TE/Flip angle: $3.25\,\mathrm{ms}/1.12\,\mathrm{ms}/10°$; Matrix: 256×192; FOV: 280×210 (with 75% rectangular FOV); a slab of 16 partitions of $3.5\,\mathrm{mm}$ thickness; temporal resolution: 6 s/slab over approximately $5\,\mathrm{min}$). A power injector (Medrad, Indianola, USA) is used to provide a bolus injection of Gd-DTPA (Dotarem, Guerbet, Roissy, France) at a dose of $0.2\,\mathrm{ml}$ Gd-DTPA/kg of body weight. The acquisition starts before the bolus injection to obtain pre-contrast volumes.

These DCE-MRI sequences are resampled using the spatial information of the T_2-W-MRI and any missing data are added using linear interpolation. The volumes of the DCE-MRI dynamic are rigidly registered to remove any patient motion during the acquisition. Furthermore, a non-rigid registration is performed between the T_2-W-MRI and DCE-MRI to propagate the prostate zones and PCa ground-truths. The resampling is implemented in C++ using the Insight Segmentation and Registration Toolkit [22].

B. Implementation

The implementation of the registration (C++), normalization (Python), and classification pipeline (Python) are publicly available on GitHub[1] [23]. The data used in this work are also publicly available[2] [24].

IV. Experiments and results

A. Goodness of model fitting

The parameter estimations from the quantification methods are related to fit a specific model to the DCE-MRI data.

[1]https://github.com/I2Cvb/lemaitre-2016-nov/tree/master
[2]https://zenodo.org/record/61163

TABLE I
COEFFICIENT OF DETERMINATION R^2 (I.E., μ ($\pm\sigma$)), WHILE FITTING DATA WITH THE DIFFERENT QUANTIFICATION MODELS.

Data type	Brix	Hoffmann	Tofts population AIF	Tofts patient AIF	PUN	Huisman
Un-normalized	0.85 ($\pm$0.11)	0.81 ($\pm$0.17)	0.84 ($\pm$0.14)	0.88 ($\pm$0.12)	0.27 ($\pm$0.18)	0.64 ($\pm$0.24)
Normalized	0.92 ($\pm$0.05)	0.72 ($\pm$0.32)	0.92 ($\pm$0.06)	0.90 ($\pm$0.10)	0.28 ($\pm$0.20)	0.75 ($\pm$0.20)

Therefore, the coefficient of determination R^2 reports the goodness of fit, as follows:

$$R^2 = 1 - \frac{\sum_{t=1}^{T}(s_t - \hat{s}_t)^2}{\sum_{t=1}^{T}(s_t - \bar{s})^2}, \tag{15}$$

where s_t and $\hat{s}_t$ are the signal to be fitted and the estimated signal at time t, respectively, and $\bar{s}$ is the average signal to be fitted.

The mean and the standard-deviation of the coefficient of determination, R^2, are reported in Table I for each quantification model. Brix, Hoffmann, and Tofts models are fitted with a coefficient R^2 superior to 0.80. Additionally, the proposed PUN model does not to fit the data well. After introspection of the fitted curves, the original model — as formulated in Eq. (12) — does not provide enough degrees of freedom to fit well the data. Additional parameters should be integrated in this model to control the translation and amplitude of the model to be fitted. Data normalization improves the coefficient R^2 for all the methods except for the Hoffmann model. The large standard deviation for this model might imply that there are some cases where the fitting fails.

B. PCa detection using pharcokinetic, semi-quantitative, and entire enhanced signal

To study the potential benefit of our normalization, PCa is detected at a voxel level using pharmacokinetic parameters estimated from non-normalized and normalized DCE-MRI data. Each individual pharmacokinetic parameter is classified to evaluate its individual discriminative power to detect PCa. In addition, p-values (p) are computed to identify pairs of classifiers which are significantly different, using a Wilcoxon signed-ranked test. Those p-values are represented in the color coded co-occurrence matrix shown in Fig. 7, where blue cells correspond to lower p-values while red cells are greater p-values. Therefore, a Random Forest (RF) classifier is used in conjunction with a Leave-One-Patient-Out Cross-Validation (LOPO CV). The use of RF is encouraged since it leads to the best performance in the state-of-the-art methods [3, 25]. The results are summarized in Table II in terms of the Area Under the Curve (AUC). Normalization can improve the detection of PCa, but the benefit of normalization is more obvious with the combination of the pharmacokinetic features of a given model (e.g., A, k_ep, and k_el for the Brix model) as previously executed in the traditional CAD system [3]. For the latter configuration, results are summarized by performing a Receiver Operating Characteristic (ROC) analysis and computing the AUC, as reported in Fig. 6. Quantification using normalized data outperforms quantification using non-normalized data in terms of the classification performance, except for Hoffmann and Tofts population-based AIF models. The reasons behind the decrease of the AUC might be related to: (i) a poor fitting as discussed in Sect. IV-A (cf., Hoffmann model) and (ii) a small number of patients for the estimation of some parameters (cf., Tofts model). The best classification performance is obtained using the semi-quantitative approach with an AUC of 0.655 ± 0.106.

As stated in the introduction, the quantification methods extract a set of parameters that characterize the enhancement of the DCE-MRI signal. However, this extraction might lead to a loss of information. This experiment is performed to assess whether using the whole DCE-MRI signal, rather than just the pharmacokinetic parameters, can improve the classification performance. Therefore, each enhanced DCE-MRI signal, normalized and un-normalized, is classified using a RF classifier in a LOPO CV fashion. The ROC analysis and AUC are reported in Fig. 6c. Classification without normalization leads to the worst performance, with an AUC of 0.568 ± 0.162. However, data normalization in conjunction with the use of the entire DCE-MRI signal is the strategy that outperforms others, with an AUC of 0.666 ± 0.154. Comparable outcomes are visible while analyzing the AUC scores distribution for each prostate zone as shown in Fig. 8. The AUC scores related to PCa in CG improves using normalized data, for most of the models.

V. DISCUSSIONS

The experiments conducted in the previous section can incite several discussions. In Tofts quantification, two different approaches have been used to infer the pharmacokinetic parameters: using a population-based or a patient-based AIF. The patient-based AIF approach leads to better classification performance. However, there are two shortcomings to take into account when considering this fact: (i) the T_{10} parameter has been fixed and is not computed from a T_1 map and (ii) the population-based AIF has been estimated from a cohort of only 17 patients. These two limitations have to be considered when asserting that population-based AIF modeling outperforms patient-based AIF modeling.

The best classification performance is achieved by normalizing the DCE-MRI data and using the entire enhanced signal as a feature, emphasizing the fact that a *loss of information* may occur while extracting quantitative parameters. Furthermore, normalization is a less complex process than all quantification methods and significantly improves the classification performance of the semi-quantitative approach ($p = 0.001$) proposed by Huisman et al.. Additionally, our normalization improves the AUC score related to the detection of PCa in CG, also known to be the most challenging cases in the diagnosis of PCa.

TABLE II
AUC (I.E., μ ($\pm\sigma$)) FOR EACH INDIVIDUAL PHARMACOKINETIC PARAMETER USING A RF CLASSIFIER.

Features	Un-normalized data	Normalized data
Brix model		
A	0.540 ($\pm$0.069)	0.555 ($\pm$0.080)
k_{el}	0.549 ($\pm$0.062)	0.577 ($\pm$0.093)
k_{ep}	0.506 ($\pm$0.032)	0.497 ($\pm$0.019)
Hoffmann model		
A	0.516 ($\pm$0.020)	0.508 ($\pm$0.031)
k_{el}	0.545 ($\pm$0.066)	0.529 ($\pm$0.065)
k_{ep}	0.550 ($\pm$0.063)	0.545 ($\pm$0.060)
Tofts model with population AIF		
K_{trans}	0.556 ($\pm$0.086)	0.565 ($\pm$0.097)
k_{ep}	0.506 ($\pm$0.026)	0.528 ($\pm$0.038)
v_p	0.533 ($\pm$0.064)	0.548 ($\pm$0.082)
Tofts model with patient AIF		
K_{trans}	0.563 ($\pm$0.077)	0.548 ($\pm$0.060)
k_{ep}	0.492 ($\pm$0.025)	0.491 ($\pm$0.020)
v_p	0.530 ($\pm$0.069)	0.495 ($\pm$0.033)
PUN model		
a_0	0.521 ($\pm$0.040)	0.530 ($\pm$0.045)
r	0.550 ($\pm$0.085)	0.573 ($\pm$0.097)
β	0.531 ($\pm$0.051)	0.549 ($\pm$0.068)
Semi-quantitative analysis		
wash-in	0.587 ($\pm$0.107)	0.533 ($\pm$0.032)
wash-out	0.516 ($\pm$0.037)	0.486 ($\pm$0.035)
IAUC	0.506 ($\pm$0.048)	0.513 ($\pm$0.032)
τ	0.565 ($\pm$0.104)	0.537 ($\pm$0.089)
$S_M - S_0$	0.560 ($\pm$0.083)	0.532 ($\pm$0.029)

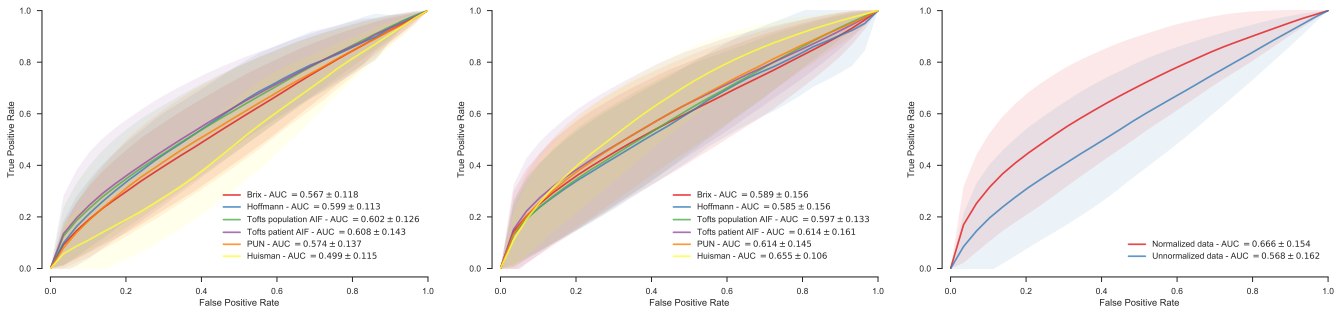

(a) Quantiative model without normalization. (b) Quantitative model With normalization. (c) Entire enhanced DCE signal classification.

Fig. 6. ROC analysis using a RF classifier with and without normalization using different approaches: (a) - (b) pharmacokinetic and semi-quantitative models without and with normalization, respectively; (c) entire enhanced DCE-MRI signal.

However, using the entire enhanced signal in conjunction with the normalization is limited by one drawback: the training time of the RF classifier increases; instead of using 3 to 5 features, so the feature space becomes a 40 dimensional space. The extraction of the semi-quantitative parameters leads to a comparable classification performance — 0.655 ± 0.108 vs. 0.666 ± 0.154 — and should be chosen as the alternative method to consider if the number of feature in the classification is critical. Despite this fact, the benefit of our proposed normalization method has been shown for both methods.

Nevertheless, this study is performed on a small cohort of patients using a single MRI machine. Generalizing the results of this study onto a larger dataset acquired from different commercial systems needs to be considered to study the robustness of the proposed approach. Additionally, our method being non-parametric should provide an adequate framework to process DCE data from different institutions, scanners with different settings.

VI. CONCLUSIONS AND FUTURE WORKS

In this work, we presented a new method for normalizing/standardizing DCE-MRI data. This method is designed to reduce the inter-patient variations that occur during data acquisition. A graph-based approach was used to correct intensity offset along with a model-based correction to reduce time offset and intensity scaling. We show the benefit of our normalization method prior to extract quantitative and semi-quantitative features, with a significant improvement of the classification performance. Nevertheless, we also show that using the whole normalized DCE-MRI signal outperforms all quantitative approaches.

In future research, this normalization needs to be part of an mp-MRI CAD system in which the DCE-MRI modality needs to be combined with other complementary modalities.

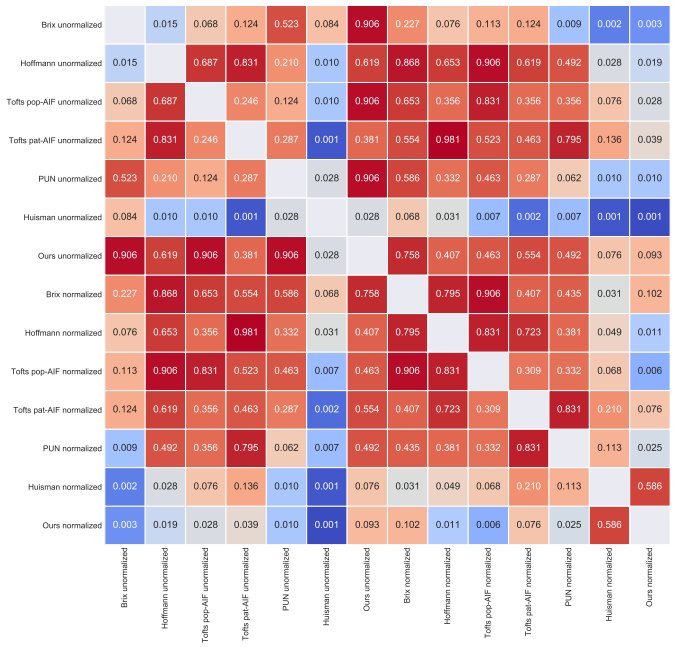

Fig. 7. Wilcoxon signed-ranked test to compare each pair of classifiers. The annotation in the matrix corresponds to the p-values (p). $p < 0.05$ indicates that a pair of classifiers are significantly different, consequently the classifier with the highest AUC significantly outperforms the other one. In the co-occurrence matrix, blue cells correspond to lower p while red cells are representing greater p.

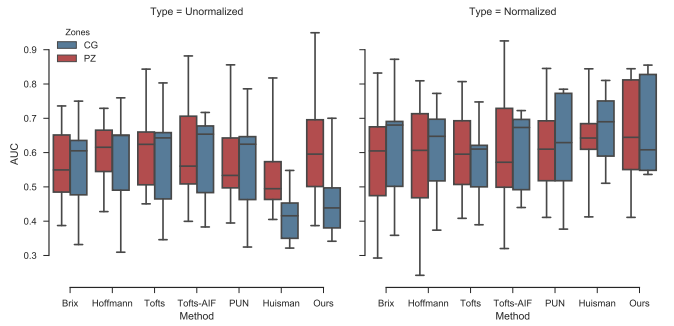

Fig. 8. Comparison of the distribution of the AUC score for each prostate zone, with and without normalization.

APPENDIX A
CONVERSION FROM FLASH SIGNAL TO MEDIA CONCENTRATION

In this appendix, we show the demonstration used to extract the agent concentration from the MRI signal.

The signal equation in FLASH sequence [26] is defined as:

$$s(t) = S_{eq} \sin\alpha \cdot \frac{1 - \exp\left(-TR\left(R_{10} + r_1 c(t)\right)\right)}{1 - \cos\alpha \cdot \exp\left(-TR\left(R_{10} + r_1 c(t)\right)\right)}, \tag{16}$$

where $s(t)$ is the MRI signal, S_{eq} is the maximum signal amplitude of the spoiled gradient at the TE which is proportional to the Proton Density (PD), α is the flip angle, TR is the Repetition Time (TR), R_{10} is the pre-contrast tissue relaxation time also equal to $\frac{1}{T_{10}}$, r_1 is the relaxitivity coefficient of the contrast agent, and $c(t)$ is the media concentration.

Therefore, the pre-contrast signal prior to bolus injection of the media is defined as:

$$S_0 = S_{eq} \sin\alpha \cdot \frac{1 - \exp\left(-TR \cdot R_{10}\right)}{1 - \cos\alpha \cdot \exp\left(-TR \cdot R_{10}\right)}. \tag{17}$$

To simplify the demonstration, let us define:

$$A = \exp(-TR \cdot R_{10}),$$
$$B = \exp(-TR \cdot r_1 c(t)).$$

Let us define:

$$S^* = \frac{S_0}{S_{eq} \sin\alpha}, = \frac{1 - A}{1 - A\cos\alpha}.$$

Thus,

$$S^* \frac{s(t)}{S_0} = \frac{S_0}{S_{eq}\sin\alpha}\frac{s(t)}{S_0}, = \frac{1 - AB}{1 - AB\cos\alpha}.$$

Now, let us define:

$$\begin{aligned}
\frac{1 - \cos\alpha \cdot S^* \frac{s(t)}{S_0}}{1 - S^* \frac{s(t)}{S_0}} &= \frac{1 - \cos\alpha\left(\frac{1-AB}{1-AB\cos\alpha}\right)}{1 - \frac{1-AB}{1-AB\cos\alpha}}, \\
&= \frac{1 - AB\cos\alpha - \cos\alpha(1 - AB)}{1 - AB\cos\alpha - (1 - AB)}, \\
&= \frac{1 - AB\cos\alpha - \cos\alpha + AB\cos\alpha}{1 - AB\cos\alpha - 1 + AB}, \\
&= \frac{1 - \cos\alpha}{AB(1 - \cos\alpha)}, \\
&= \frac{1}{AB}.
\end{aligned}$$

Thus,

$$-TR \cdot R_{10} - TR \cdot r_1 c(t) = \ln\left(\frac{1 - \cos\alpha \cdot S^* \frac{s(t)}{S_0}}{1 - S^* \frac{s(t)}{S_0}}\right).$$

Therefore,

$$c(t) = \frac{1}{TR \cdot r_1} \ln\left(\frac{1 - \cos\alpha \cdot S^* \frac{s(t)}{S_0}}{1 - S^* \frac{s(t)}{S_0}}\right) - \frac{R_{10}}{r_1}. \tag{19}$$

ACKNOWLEDGMENT

Guillaume Lemaître is supported by the Generalitat de Catalunya (grant nb. FI-DGR2012) and partly by the Mediterranean Office for Youth (grant nb. 2011/018/06).

REFERENCES

[1] J. Ferlay, H.-R. Shin, F. Bray, D. Forman, C. Mathers, and D. M. Parkin, "Estimates of worldwide burden of cancer in 2008: Globocan 2008," *International journal of cancer*, vol. 127, no. 12, pp. 2893–2917, 2010.

[2] J. C. Weinreb, J. O. Barentsz, P. L. Choyke, F. Cornud, M. A. Haider, K. J. Macura, D. Margolis, M. D. Schnall, F. Shtern, C. M. Tempany *et al.*, "Pi-rads prostate imaging–reporting and data system: 2015, version 2," *European urology*, vol. 69, no. 1, pp. 16–40, 2016.

[3] G. Lemaître, R. Martí, J. Freixenet, J. C. Vilanova, P. M. Walker, and F. Meriaudeau, "Computer-aided detection and diagnosis for prostate cancer based on mono and multi-parametric mri: A review," *Computers in biology and medicine*, vol. 60, pp. 8–31, 2015.

[4] G. Brix, W. Semmler, R. Port, L. R. Schad, G. Layer, and W. J. Lorenz, "Pharmacokinetic parameters in cns gd-dtpa enhanced mr imaging." *Journal of computer assisted tomography*, vol. 15, no. 4, pp. 621–628, 1991.

[5] P. S. Tofts, B. Berkowitz, and M. D. Schnall, "Quantitative analysis of dynamic gd-dtpa enhancement in breast tumors using a permeability model," *Magnetic Resonance in Medicine*, vol. 33, no. 4, pp. 564–568, 1995.

[6] M. Heilmann, F. Kiessling, M. Enderlin, and L. R. Schad, "Determination of pharmacokinetic parameters in dce mri: consequence of nonlinearity between contrast agent concentration and signal intensity," *Investigative radiology*, vol. 41, no. 6, pp. 536–543, 2006.

[7] A. Gliozzi, S. Mazzetti, P. P. Delsanto, D. Regge, and M. Stasi, "Phenomenological universalities: a novel tool for the analysis of dynamic contrast enhancement in magnetic resonance imaging," *Physics in medicine and biology*, vol. 56, no. 3, pp. 573–586, 2011.

[8] H. J. Huisman, M. R. Engelbrecht, and J. O. Barentsz, "Accurate estimation of pharmacokinetic contrast-enhanced dynamic mri parameters of the prostate," *Journal of Magnetic Resonance Imaging*, vol. 13, no. 4, pp. 607–614, 2001.

[9] G. Lemaitre, M. R. Dastjerdi, J. Massich, J. C. Vilanova, P. M. Walker, J. Freixenet, A. Meyer-Baese, F. Mériaudeau, and R. Marti, "Normalization of t2w-mri prostate images using rician a priori," in *SPIE Medical Imaging*. International Society for Optics and Photonics, 2016, pp. 978 529–978 529.

[10] U. Hoffmann, G. Brix, M. V. Knopp, T. Heβ, and W. J. Lorenz, "Pharmacokinetic mapping of the breast: a new method for dynamic mr mammography," *Magnetic resonance in medicine*, vol. 33, no. 4, pp. 506–514, 1995.

[11] R. Meng, S. D. Chang, E. C. Jones, S. L. Goldenberg, and P. Kozlowski, "Comparison between population average and experimentally measured arterial input function in predicting biopsy results in prostate cancer," *Academic radiology*, vol. 17, no. 4, pp. 520–525, 2010.

[12] J. Chen, J. Yao, and D. Thomasson, "Automatic determination of arterial input function for dynamic contrast enhanced mri in tumor assessment," in *International Conference on Medical Image Computing and Computer-Assisted Intervention*. Springer, 2008, pp. 594–601.

[13] Y. Zhu, M.-C. Chang, and S. Gupta, "Automated determination of arterial input function for DCE-MRI of the prostate," in *SPIE Medical Imaging*. International Society for Optics and Photonics, 2011, pp. 79 630W–79 630W.

[14] D. Shanbhag, S. N. Gupta, K. Rajamani, Y. Zhu, and R. Mullick, "A generalized methodology for detection of vascular input function with dynamic contrast enhanced perfusion data," in *ISMRM*, vol. 12, 2012, p. 10.

[15] F. M. Fennessy, A. Fedorov, T. Penzkofer, K. W. Kim, M. S. Hirsch, M. G. Vangel, P. Masry, T. A. Flood, M.-C. Chang, C. M. Tempany *et al.*, "Quantitative pharmacokinetic analysis of prostate cancer dce-mri at 3t: comparison of two arterial input functions on cancer detection with digitized whole mount histopathological validation," *Magnetic resonance imaging*, vol. 33, no. 7, pp. 886–894, 2015.

[16] M. C. Schabel and D. L. Parker, "Uncertainty and bias in contrast concentration measurements using spoiled gradient echo pulse sequences," *Physics in medicine and biology*, vol. 53, no. 9, pp. 2345–2373, 2008.

[17] C. M. De Bazelaire, G. D. Duhamel, N. M. Rofsky, and D. C. Alsop, "Mr imaging relaxation times of abdominal and pelvic tissues measured in vivo at 3.0 t: preliminary results 1," *Radiology*, vol. 230, no. 3, pp. 652–659, 2004.

[18] J. C. Carr and T. J. Carroll, *Magnetic resonance angiography: principles and applications*. Springer Science & Business Media, 2011.

[19] G. J. Parker, C. Roberts, A. Macdonald, G. A. Buonaccorsi, S. Cheung, D. L. Buckley, A. Jackson, Y. Watson, K. Davies, and G. C. Jayson, "Experimentally-derived functional form for a population-averaged high-temporal-resolution arterial input function for dynamic contrast-enhanced mri," *Magnetic resonance in medicine*, vol. 56, no. 5, pp. 993–1000, 2006.

[20] D. C. Sorensen, "Newton's method with a model trust region modification," *SIAM Journal on Numerical Analysis*, vol. 19, no. 2, pp. 409–426, 1982.

[21] V. Giannini, S. Mazzetti, A. Vignati, F. Russo, E. Bollito, F. Porpiglia, M. Stasi, and D. Regge, "A fully automatic computer aided diagnosis system for peripheral zone prostate cancer detection using multi-parametric magnetic resonance imaging," *Computerized Medical Imaging and Graphics*, vol. 46, pp. 219–226, 2015.

[22] M. M. McCormick, X. Liu, L. Ibanez, and J. Jomier, "Itk: enabling reproducible research and open science," *Frontiers in neuroinformatics*, vol. 8, p. 13, 2014.

[23] G. Lemaitre, "lemaitre-2016-nov: 0.1.1," Sep. 2016. [Online]. Available: http://dx.doi.org/10.5281/zenodo.61612

[24] G. Lemaitre, R. Martí, and F. Meriaudeau, "DCE-MRI prostate images," Aug. 2016. [Online]. Available: http://dx.doi.org/10.5281/zenodo.61163

[25] G. Litjens, O. Debats, J. Barentsz, N. Karssemeijer, and H. Huisman, "Computer-aided detection of prostate cancer in mri," *IEEE transactions on medical imaging*,

vol. 33, no. 5, pp. 1083–1092, 2014.

[26] A. Haase, J. Frahm, D. Matthaei, W. Hanicke, and K.-D. Merboldt, "Flash imaging. rapid nmr imaging using low flip-angle pulses," *Journal of Magnetic Resonance (1969)*, vol. 67, no. 2, pp. 258–266, 1986.

Guillaume Lemaitre G. Lemaitre received B.Sc. degree (Hons) in electrical, signal, and image engineering from the Universté de Bourgogne and the M.Sc. Erasmus Mundus Master of Excellence (Hons) in Vision and Robotics co-jointly delivered by the Université de Bourgogne, Universitat de Girona, and Heriot-Watt University. Additionally, he received a M.Sc. in Business Innovation and Technology Management by the Universitat de Girona. He got a joint Ph.D. from the Université de Bourgogne and the Universitat de Girona. He is currently working for the Center for Data Sciences Paris-Saclay and for the PARIETAL team of the Inria Saclay. His research interests include machine learning applied to pluridisciplinary fields as medical imaging.

Fabrice Mériaudeau F. Mériaudeau was born in Villeurbanne, France, on March 18, 1971. He received both the master degree in physics at Dijon University, France as well as an Engineering Degree (FIRST) in material sciences in 1994. He also obtained a Ph.D. in image processing at the same University in 1997. He was a postdoc for a year at The Oak Ridge National Laboratory. He is currently "Professeur des Universite" and was Director of the Le2i (UMR CNRS), which has more than 200 staff members, from 2011 to 2016. His research interests were focused on image processing for non-conventional imaging systems (UV, IR, polarization) and more recently on medical/biomedical imaging. He has coordinated an Erasmus Mundus Master in the field of Computer Vision and Robotics from 2006 to 2010 and he was the Vice President for International Affairs for the University of Burgundy from 2010 to 2012. He has authored and co-authored more than 150 international publications and holds three patents. Since 2016, he has joined Universiti Teknologi PETRONAS as a professor.